修 士 論 文

題 目

Broadband frequency entangled photon generation using silicon nitride ring cavities

指導教員　　竹 内　繁 樹　教授

京都大学大学院工学研究科　電子工学専攻

氏 名　　　殷　政浩

令和2年2月1日

Broadband frequency entangled photon generation using silicon nitride ring cavities

Zhenghao Yin

Abstract

Lorem ipsum dolor sit amet, consectetuer adipiscing elit. Ut purus elit, vestibulum ut, placerat ac, adipiscing vitae, felis. Curabitur dictum gravida mauris. Nam arcu libero, nonummy eget, consectetuer id, vulputate a, magna. Donec vehicula augue eu neque. Pellentesque habitant morbi tristique senectus et netus et malesuada fames ac turpis egestas. Mauris ut leo. Cras viverra metus rhoncus sem. Nulla et lectus vestibulum urna fringilla ultrices. Phasellus eu tellus sit amet tortor gravida placerat. Integer sapien est, iaculis in, pretium quis, viverra ac, nunc. Praesent eget sem vel leo ultrices bibendum. Aenean faucibus. Morbi dolor nulla, malesuada eu, pulvinar at, mollis ac, nulla. Curabitur auctor semper nulla. Donec varius orci eget risus. Duis nibh mi, congue eu, accumsan eleifend, sagittis quis, diam. Duis eget orci sit amet orci dignissim rutrum.

Contents

Chapter 1

Introduction

The flying qubit—photon—featuring the advantages of long coherent time and multiple degrees of freedom (DoF), is a promising candidate in quantum computation and quantum communication. However, in the term of DoF, much of research up to now focuses on the photon polarization and path entanglement realization, very little attention has been paid to the role of frequency entanglement, which is continuous and infinite in hilbert space.

Furthermore, the previous research shows that frequency entangled photon pairs can be exploited not only in wavelength division multiplexing quantum key distribution [1] but also transferring quantum information in future quantum networks [2]. Besides, in recent applications of quantum metrology, quantum optical coherent tomography (QOCT), the broadband frequency entanglement [3] is also required.

1.1 BACKGROUND

Compared with crystal experiments, a chip-scale photon source has the advantages of scalability and robustness. A conventional material candidate is silicon on insulator (SOI), since it is CMOS-compatible and supplied by a lot of wafer manufacturers. However, suffering from two photon absorption and stimulated Raman scattering, silicon is no able to generate broadband frequency conversion. Since that, silicon nitride, which is transparent from visible to near infrared range, is preferred to perform broadband frequency entanglement. A recent record is single pair from visible to telecom band [4].

1.2   OBJECTIVE

In the platform of silicon nitride, we utilize the third-order optical nonlinearity and confine the light in the sub-micron scale—optical waveguides. To enhance the nonlinear interaction, we define the ring resonator and couple the light inside along with a bus waveguide. The broadband property is ensured by carefully optimizing the device geometry to achieve a broadband phase matching condition. All the photon pair generation events are detected by single photon detectors and verified by the coincident counting.

In this dissertation, the terms 'broadband photon pair' is used to describe that pairs are generated in different frequency pairs simultaneously and but entangled only in the single mode pair.

1.3   OUTLINE

The following chapters are sequentially divided in different topics.

Chapter 2

Principal theory

The way how light travels in a chip-scale is remarkably different the way in free-space. In the sub-micron scale, the electromagnetic wave can only propagate in a fewer cycles due to the constraint of material boundaries. However, since atoms and molecules are much smaller, the refractive index is not changed, as well as the reflection, interference and diffraction.

Based on these facts, in order to perform quantum optics experiments *at the bottom*, first, we shall confine the light propagation in a specific waveguide. On the other hand, thanks to modern laser technology, nonlinear optics is involved and give birth to optical frequency conversion. To enhance these nonlinear optical phenomena, we adopt the cavity structure and achieve sizable control.

In this chapter, we briefly introduce the guided wave theory and then move the cavity structure, ring resonators. Next, the nonlinear optics, in particular third-order nonlinear processes, is discussed in the following section. Although the quantum nature of photon pair generation distinct from the classical theory, all the physics mentioned above are necessary to analyse our essential research object, the silicon nitride ring resonators.

2.1 Guided-wave optics

In an ideal optical waveguide, the core layer and the cladding layer are usually composed of two different materials, where the refractive index is larger in the core. As an analogue of optical fibers, only in the higher index region can the light propagate, and meanwhile dissipate in a wavelength scale in the lower index region.

Usually, we assume the core and the cladding layer are made of nonmagnetic (magnetic permeability $\mu = \mu_0$) and dielectric material (conductivity $\sigma = 0$). Furthermore, we neglect the nonlinear response of the polarization of electric field ($\mathbf{P} \simeq \varepsilon_0 \chi \mathbf{E}$).

Since the waveguide in numerous research objects, is deposited or sputtered using chemical or physical methods, the uneven density in the waveguide layer can not be negligible. Hence, the propagation equation derived from Maxwell's equation is

$$(\nabla_\perp^2 + k^2 n^2 - \beta^2)\mathbf{E} = -(\nabla_\perp + i\beta\hat{\mathbf{z}})(\mathbf{E}_\perp \cdot \nabla_\perp \ln n^2) \tag{2.1}$$

where $\perp$ denotes the transverse component, $\nabla_\perp^2 = \nabla_x^2 + \nabla_y^2$. And k, n, β are the wave vector in vacuum, refractive index and propagation constant, respectively. While, with the negligible film anisotripy, Equation 2.1 can be approximated into

$$(\nabla_\perp^2 + k^2 n^2 - \beta^2)\mathbf{E} = 0 \tag{2.2}$$

This is the normal *Helmholtz equation*, indicating the relation between propagation constant β and material refractive index, i.e. *chromatic dispersion*.

Next, the boundary conditions determining the solution to Eqn. 2.2, arise from the Maxwell's equations as well.

$$\begin{aligned} \hat{\mathbf{n}} \cdot (\mathbf{E_a} - \mathbf{E_b}) &= 0 \\ \hat{\mathbf{n}} \times (\mathbf{H_a} - \mathbf{H_b}) &= 0 \end{aligned}$$

which is the continuity condition of both electric and magnetic field at all dielectric material interfaces. Here, $\hat{\mathbf{n}}$ is the normal direction at the material boundary and the subscript a, b denote different regions.

2.1.1 Waveguide modes

In the case of channel waveguides, the index discontinuity from both vertical and horizontal sides can be decomposed into two sets of independent and complete conditions, i.e. the horizontal boundary condition and vertical boundary condition, with the discontinuity on the waveguide corners neglected. In other words, approximately the equation has two independent partiuclar solutions, which is the mathematical origin of *transverse electric* (TE) modes and *transverse magnetic* (TM) modes.

Hence, we can study the eigenequantion by selecting only one set of boundary condition, as used in the *the effective index method*. For example, in a planar waveguide shown in Figure 8.1 ,$\mathrm{d}^2/\mathrm{d}y^2 = 0$[1], the TE mode features $E_x = 0$ and consider only y-component,

$$\frac{\mathrm{d}^2 E_y}{\mathrm{d}x^2} + (k^2 n^2 - \beta^2) E_y = 0 \tag{2.3}$$

and E_y is continous at $x = \pm d/2$, where d is the thickness of core layer.

For the region $|x| > d/2$, the light evanesces at x-direction at rate κ and in contrast, in the region of core layer, the light performs like stationary wave, denoting with k_x. By substituting these conditions, phase continuity is achieved between two interface

$$2k_x d = m\pi + 2\arctan(\kappa/k_x) \tag{2.4}$$

where m is the index of stationary wave. The second term can be treated as the Goos-Hänchen phase shift. Overall, the waveguide modes characterize that the phase shall maintain itself with an $m\pi$ shift along with the shift at the boundaries.

In the case of TM modes, the eigen equation is

$$2k_x d = m\pi + 2\arctan(\delta\kappa/k_x) \tag{2.5}$$

where $\delta = n_a/n_b$ is the index ratio and only differs from Equation 2.4 with this parameter. conclusively, the less is δ parameter, the propagation constant of TE and TM modes are closer.

2.1.2 Dispersion relation

Based on Equation 2.4 and Equation 2.5, k_x can be solved and then utilized to calculate propagation constant β, since $n_a^2 k^2 = k_\perp^2 + \beta^2$. In the case of channel waveguides, the TE and TM solutions are both necessary. Therefore, propagation constants β can be expressed as the product of free space wave vector k and the *effective index* n_{eff}

$$\beta = n_{\text{eff}} k = n_{\text{eff}}(\lambda) \frac{2\pi}{\lambda} = n_{\text{eff}}(\omega) \frac{\omega}{c} \tag{2.6}$$

---

[1]Since the planar waveguide is infinite at the y-direction , thus the solution is identical in arbitrary xz-plane, which means no gradient along x-axis.

along with the differential form

$$\frac{\mathrm{d}\beta}{\mathrm{d}k} = n_{\text{eff}} + k\frac{\mathrm{d}n_{\text{eff}}}{\mathrm{d}k} = n_{\text{eff}} - \lambda\frac{\mathrm{d}n_{\text{eff}}}{\mathrm{d}\lambda} \equiv n_g \tag{2.7}$$

$$\frac{\mathrm{d}\omega}{\mathrm{d}\beta} = c\frac{\mathrm{d}k}{\mathrm{d}\beta} = \frac{c}{n_g} \equiv v_g \tag{2.8}$$

which defines the group index n_g and group velocity v_g.

This formula linking $\beta - k$ or $\beta - \omega$ is named as dispersion relation, which gives the physics that light with different color propagates at different *speed*. Furthermore, Equation 2.4 and Equation 2.5 also indicate that the dispersion relation intrinsically depends on waveguide geometry.

2.2 RING RESONATORS

The ring resonators comprise of a bus waveguide and a ring waveguide, are usually demonstrated as optical filters or modulators at a wide range of platforms. The working principle of ring resonator can be derived completely [5] as an analogue to Fabry-Pérot etalon, based on the coupling mode theory.

In the model illustrated in Figure 8.2, the self-coupling coefficient τ and the cross-coupling coefficient κ can be evaluated analytically or using numerical simulation. Assuming the coupling only occur at the very close area, τ, κ are the power splitting ratios of the coupler and satify $\tau^2 + \kappa^2 = 1$ if the coupling section is lossless. a is the single-pass amplitude transmission, including both propagation loss in the ring and loss in the couplers.

The transmission rate of a all-pass type ring cavity takes the form of

$$T = \frac{I_{\text{pass}}}{I_{\text{input}}} = \frac{a^2 - 2a\tau\cos\phi + \tau^2}{1 - 2ar\cos\phi + a^2\tau^2} \tag{2.9}$$

where $\phi = \beta L$ is the phase shift in a single round trip.

2.2.1 Coupling condition

By plotting the function in Figure 8.3, we can see, the extinction ratio of absorption peak is defined by the self-coupling coefficient τ and the single-pass amplitude transmission a due to device geometric differences, like the gap between the bus waveguide and the

ring cavity. Namely, a and τ both determine the coupling condition, which can be categorized in three cases

- **weak coupling** $a > \tau$. The loss inside the ring is larger than the power coupled from bus waveguides.

- **critical coupling** $a = \tau$. The loss and self-coupling are in balance. The optical power restored in the resonator achieve the minimum.

- **over coupling or strong coupling** $a < \tau$. The coupling is too strong for the light to dissipate in a single round trip.

Previous work [6] proposed a method to evaluate the coupling condition above using the experimentally measured device transmission. Considering the loss in the coupler, bent segment of ring and higher mode perturbance, usually the critical coupling varies from modes and the cross section of waveguides [7].

2.2.2 Spectrum characteristics

Meanwhile, the minimum of transmission rate T can be achieved periodically as $\phi = 2m\pi$, which defines the resonance of ring resonators. Therefore, the resonance condition is derived as

$$\beta L = 2m\pi \qquad (2.10)$$

where m is the mode index. Specifically, the propagation constant β, shall be an integral times of a quasi wave vector $2\pi/L$. With this condition, the free spectral range (FSR) of wavelength and frequency are obtained

$$\Delta\lambda_{\text{FSR}} \approx \frac{\lambda_{\text{res}}^2}{n_g L} \qquad (2.11)$$

$$\Delta\omega_{\text{FSR}} \approx \frac{2\pi c}{n_g L} \qquad (2.12)$$

In both wavelength and frequency domain, FSR determines the spacing of neighbouring resonant peak. This is a significant factor when the ring resonators are designed.

Furthermore, from Equation 2.9, the full width at half maximum (FWHM) of the resonance spectrum is derived as $\delta\lambda$

$$\delta\phi = \frac{2(1 - a\tau)}{\sqrt{\tau a}} \qquad (2.13)$$

Likely, since the phase ϕ is related with the wave vector k in Equation 2.7. Substituting $\delta\phi = Ln_g\delta k$, the half width of wavelength is

$$\delta\lambda = \frac{\mathrm{d}\lambda}{\mathrm{d}k}\delta k = \frac{\lambda_{\mathrm{res}}^2}{2\pi Ln_g}\frac{2(1 - a\tau)}{\sqrt{\tau a}} \tag{2.14}$$

the same, at the frequency domain

$$\delta\omega = \frac{\mathrm{d}\omega}{\mathrm{d}k}\delta k = \frac{c}{Ln_g}\frac{2(1 - a\tau)}{\sqrt{\tau a}} \tag{2.15}$$

Note in Equation 2.11 Equation 2.12 Equation 2.14 and Equation 2.15, the group index n_g is explicit instead of the effective index n_{eff} because both free spectral range and full width depend on the differential form, Equation 2.7.

And the finesse F of the resonator is defined

$$F \equiv \frac{2\pi}{\delta\phi} = \frac{\pi\sqrt{\tau a}}{2(1 - a\tau)} \tag{2.16}$$

Finally, we define the quality factor, a measure of the sharpness of the resonance relative to its central frequency.

$$Q = \frac{\lambda_{\mathrm{res}}}{\delta\lambda} = \frac{\pi Ln_g\sqrt{\tau a}}{\lambda_{\mathrm{res}}(1 - a\tau)} \tag{2.17}$$

Usually, the Q-factor can be decomposed into two parts by formula $Q^{-1} = Q_i^{-1} + Q_l^{-1}$. And Q_i, Q_l are intrinsic Q-factor and loaded Q-factor, referring to the loss inside the ring waveguide and at the coupler, respectively. The physical meaning of the finesse and Q-factor relates to the number of round-trips before being lost to internal loss and the bus waveguides when the power is depleted to $1/e$ of its initial value.

2.3 THRID-ORDER NONLINEAR OPTICS

Although the nonlinear effect is ignored during the derivation of waveguide modes in Section 2.1, for numerous materials, the nonlinear response of electric field is significant even at mW level, which is easy to occur with assistance of modern lasers. The origin of nonlinear optic phenomena is similar to the movement of the object in a potential field, such as the ball-spring model.

In the nonlinear material, the atoms or molecules are driven by the external electric field, due to the around chemical bonds or molecular orientation, the displacement of atoms or molecules perform nonlinear dependence on the strength of field. In real-world materials, interaction coming arising from various frequency leads to the addition or subtraction of these frequency components. This explains the frequency conversion nature in nonlinear optics.

It is worth mentioning that not only in the bulk crystals, but also in the sub-micron scale [8], the nonlinear response is still efficient, even over a single-layer two-dimensional material.

Here, a brief theoretical derivation is elucidated and in the following part, degenerate four wave mixing is emphasized. In an isotropic nonlinear medium, assuming only instantaneous dielectric response, the relation between the polarization and the electric field is expressed by a power series in the electric field

$$\mathbf{P}(t) = \varepsilon_0(\chi^{(1)}\mathbf{E}(t) + \chi^{(2)}\mathbf{E}^2(t) + \chi^{(3)}\mathbf{E}^3(t)) = \varepsilon_0\chi^{(1)}\mathbf{E}(t) + \mathbf{P}_{\mathrm{NL}}(t) \tag{2.18}$$

Note in Equation 2.18, the nonlinear susceptibilities $\chi^{(2)}$ and $\chi^{(3)}$ are second-rank and third-rank tensors, corresponding to the tensor product with $\mathbf{E}^2$ and $\mathbf{E}^3$. The higher order response is neglected and sequentially, only $\chi^{(2)}$ processes and $\chi^{(3)}$ processes are to be introduced.

$\chi^{(2)}$ **processes**

In centrosymmetric crystals such as silicon, the second-order susceptibility term is absent. However, in other materials like lithium niobate ($LiNbO_3$) and aluminium nitride (AlN), the second-order nonlinearity are essential to realize electro-optic modulation and second harmonic generation.

$\chi^{(3)}$ **processes**

Silicon and silicon nitride are both cubic crystal. Due to the third-order dependence, another factor equivalent to the optical intensity is involved, the $\chi^{(3)}$ process is also named as intensity-dependent effect or Kerr effect.

Consider three frequency components of $\mathbf{E}^3$, using the complex expression of electric field

$$\mathbf{E}(\mathbf{r}, t) = \sum_{k=1}^{3} \mathbf{E}_{\omega_k}(\mathbf{r}, t) = \frac{1}{2}\sum_{k=1}^{3} \left(\mathbf{E}_{\omega_k}(\mathbf{r})e^{i\omega_k t} + c.c.\right) \tag{2.19}$$

Substituting into third-order term in Equation 2.18 and arranging with the same propagation direction, the third-order polarization is

$$\mathbf{P}^{(3)}(t) = \frac{3}{4}\varepsilon_0\chi^{(3)}\left[|\mathbf{E}_{\omega_1}|^2\mathbf{E}_{\omega_1} + \cdots\right] \qquad \text{SPM} \quad (2.20)$$

$$+ \frac{6}{4}\varepsilon_0\chi^{(3)}\left[(|\mathbf{E}_{\omega_2}|^2 + |\mathbf{E}_{\omega_3}|^2)\mathbf{E}_{\omega_1} + \cdots\right] \qquad \text{XPM} \quad (2.21)$$

$$+ \frac{1}{4}\varepsilon_0\chi^{(3)}\left[(\mathbf{E}_{\omega_1}^3 e^{i\omega_1 t} + c.c.) + \cdots\right] \qquad \text{THG} \quad (2.22)$$

$$+ \frac{3}{4}\varepsilon_0\chi^{(3)}\left[\frac{1}{2}(\mathbf{E}_{\omega_1}^2\mathbf{E}_{\omega_2} e^{i(2\omega_1+\omega_2)t} + c.c.) + \cdots\right] \qquad \text{FWM} \quad (2.23)$$

$$+ \frac{3}{4}\varepsilon_0\chi^{(3)}\left[\frac{1}{2}(\mathbf{E}_{\omega_1}^2\mathbf{E}_{\omega_2}^* e^{i(2\omega_1-\omega_2)t} + c.c.) + \cdots\right] \qquad \text{FWM} \quad (2.24)$$

$$+ \frac{6}{4}\varepsilon_0\chi^{(3)}\left[\frac{1}{2}(\mathbf{E}_{\omega_1}\mathbf{E}_{\omega_2}\mathbf{E}_{\omega_3} e^{i(\omega_1+\omega_2+\omega_3)t} + c.c.) + \cdots\right] \quad \text{FWM} \quad (2.25)$$

$$+ \frac{6}{4}\varepsilon_0\chi^{(3)}\left[\frac{1}{2}(\mathbf{E}_{\omega_1}\mathbf{E}_{\omega_2}\mathbf{E}_{\omega_3}^* e^{i(\omega_1+\omega_2-\omega_3)t} + c.c.) + \cdots\right] \quad \text{FWM} \quad (2.26)$$

In above equations, $\cdots$ stands for all possible permutation terms contributed by frequencies $\omega_1, \omega_2, \omega_3$. The abbreviation on the right side represent for

SPM, self-phase modulation

SPM adds an intensity-dependent term except the linear polarization, leading to a broadening of the pulse spectrum.

Note the $\chi^{(3)}$ is complex, thus the imaginary part may contribute to another intensity-dependent absorption mechanics, which is usually depicted in the *two-photon absorption* (TPA). The free carriers excited by TPA in further change the temporally both the absorption coefficient and the refractive index of material.

$$n = n_0 + n_2 I + i\frac{\lambda}{4\pi}(\alpha_0 + \alpha_2 I) \qquad (2.27)$$

where the I is the intensity, n_2 is the Kerr coefficient and α_0, α_2 are related with TPA-induced free carrier absorption (FCA) and free carrier index (FCI) change, both interrelated with third-order susceptibility

$$n_2 = \frac{1}{cn_0^2\varepsilon_0}\frac{3}{4}\text{Re}\{\chi^{(3)}\} \qquad (2.28)$$

$$\alpha_2 = \frac{-\omega}{c^2 n_0^2\varepsilon_0}\frac{3}{2}\text{Im}\{\chi^{(3)}\} \qquad (2.29)$$

10

A figure of merit (FOM) is often used to compare the magnitude of Kerr coefficient n_2 with the strength of the TPA coefficient α_2

$$\text{FOM} = \frac{1}{\lambda}\frac{n_2}{\alpha_2} \tag{2.30}$$

XPM, cross-phase modulation

XPM can be seen the first signal index influenced by a second signal. And the coeffiecient of XPM is twice as strong as the SPM coefficient.

THG, third-harmonic generation

Like SHG, THG generated a new frequency with is one-third of input frequency.

FWM, four wave mixing

In FWM process, more than three frequencies are involved. Nevertheless, Equation 2.23 and Equation 2.24 contain two identical wave, sometime calles as degenerate four wave mixing (DFWM). And Equation 2.25 and Equation 2.26 is a truly four wave process. Similar to the relation between SPM and XPM, the non-degenerate FWM is naturally twice stronger.

Traditionally, following the terminology in laser field, in DFWM, the ω_1 square term Equation 2.24 is labeled as pump frequency, and another two frequencies are referred to signal and idler frequency.

Besides, the imaginary part of third-order susceptibility incorporate other four-wave absorption mechanics, such as *stimulated Brillouin scatter* (SBS) and *stimulated Raman scattering* (SRS), which originate from acoustic waves in crystals and vibrating molecules.

Finally, it worth mentioning that in all THG and FWM processes, different from SPM and XPM processes, phase matching condition is required due to the complex exponential factors. In this case, the phase mismatch can change the polarization rapidly and leads to periodical variation in these parametric processes.

Chapter 3

Phase match condition for spontaneous four wave mixing in a ring cavity

According to the previous chapter, in a typical nonlinear optical waveguide or silica fibers, despite the stimulated Raman and Brillouin scattering, the frequency conversion processes involve not only the self-phase modulation of pump light and cross-phase modulation of signal and idler light, but also the phase mismatch in four wave mixing propagation factor. In this case, it is necessary to study the coupled nonlinear equations involving signal, idler and pump intensity [9].

Whereas in ring resonators, whose mode linewidth (pm) is much narrower than self-phase modulation frequency broadening, the frequency broadening in single mode is negligible. Thus the phase mismatch among cavity modes becomes the critical factor of the band of four wave mixing.

This chapter first describes the major origin of phase mismatch, chromatic dispersion, and goes on to the design philosophy used in device fabrication. Besides, several topics concerning the band of phase matching are also included.

3.1 CHROMATIC DISPERSION

In a typical FWM process, both energy conservation and momentum conservation are required

$$\beta_i + \beta_s = 2\beta_p \tag{3.1}$$

$$\omega_i + \omega_s = 2\omega_p \tag{3.2}$$

where the subscripts s i p stand for signal, idler and pump light.

Meanwhile, the resonance condition Equation 2.10 leads to $\beta = m\frac{2\pi}{L}$. Thus, Equation 3.1 is equivalent to

$$m_i + m_s = 2m_p \tag{3.3}$$

We can see that *the momentum conservation agrees with mode number conservation.* That is to say, as pump light sets into resonant wavelengths, by choosing the equidistant modes relative to the pump mode, the momentum conservation can be naturally satisfied. This is the most important difference from non-resonant devices.

Therefore, we can estimate the phase mismatch only in the frequency domain. Expand the resonant frequency into Taylor seires at ω_0 to the propagation constant β

$$
\begin{aligned}
\omega_\mu &= \omega_0 + \sum_{j=1} \frac{\mathrm{d}^j \omega}{\mathrm{d}\beta^j} \frac{(\beta - \beta_0)^j}{j!} \\
&= \omega_0 + \sum_{j=1} \frac{\mathrm{d}^j \omega}{\mathrm{d}\beta^j} \left(\frac{2\pi}{L}\right)^j \frac{\mu^j}{j!} \\
&= \omega_0 + D_1 \mu + \frac{D_2}{2!}\mu^2 + \frac{D_3}{3!}\mu^3 + \cdots
\end{aligned}
\tag{3.4}
$$

where $D_j \equiv (\frac{2\pi}{L})^j \, \mathrm{d}^j\omega/\mathrm{d}\beta^j$ are *j*-order mode number dispersion parameter, whose dimension are all T^{-1} and $\mu \in \mathbb{Z}$ is the relative mode number.

It is easy to know that $D_1/2\pi = v_g/L$ is the free spectral range in the frequency and indicates that the dispersion property is related with the difference of resonant frequencies.

Next, we introduce the integrated dispersion D_{int} [10] to analyze the phase mismatch

$$D_{\text{int}}(\mu) \equiv \omega_\mu - (\omega_0 + D_1\mu) \tag{3.5}$$

$$= \frac{D_2}{2!}\mu^2 + \frac{D_3}{3!}\mu^3 + \cdots$$

In particular, D_{int} is the residual dispersion higher than second order. Approximately, if $D_3\mu \ll D_2$, the second-order dispersion will dominate the integrated dispersion both at signal and idler mode.

Indeed, the mode number dispersion parameter is linked with the dispersion coefficients in frequency and wavelength domain, giving such a chain rule

$$D_2 = -\frac{L}{2\pi}D_1^3\beta_2 = \frac{L}{2\pi}\frac{\lambda^2}{2\pi c}D_1^3 D_\lambda \qquad (3.6)$$

where $\beta_2 = \mathrm{d}^2\beta/\mathrm{d}\omega^2$ is group velocity dispersion (GVD) and $D_\lambda = -(\lambda/c)\,\mathrm{d}^2 n/\mathrm{d}\lambda^2$ is the dispersion parameter.

In this method, we can analyze the phase mismatch in FWM quantitatively

$$\begin{aligned}\Delta\omega &\equiv \omega_s + \omega_i - 2\omega_p \qquad (3.7)\\ &= D_{\text{int}}(\mu) + D_{\text{int}}(-\mu) \\ &= 2\left(\frac{D_2\mu^2}{2!} + \frac{D_4\mu^4}{4!} + \frac{D_6\mu^6}{6!} + \cdots\right)\end{aligned}$$

From the above derivation, the frequency mismatch $\Delta\omega$ only adds to the even terms of Taylor series in Equation 3.4. To conclude, a rough presupposition to increase the efficient phase matched band is achieving zero and flat dispersion around pump wavelengths.

3.2 DISPERSION COMPENSATION

Mentioned previously in Section 2.1, the dispersion behaviour in integrated devices is not only the intrinsic material property, but also depends on the waveguide dimension.

In other words, the phase mismatch occurs as a result of material dispersion D_M and waveguide dispersion D_W, $D_\lambda = D_M + D_W$. Here, we adopt the wavelength dispersion parameter since the wavelength domain is measurable.

Usually, the Sellmeier equation is used to fit the refractive index for a particular transparent medium. Luke *et al.* reported the measured refractive index of stoichiometric Si_3N_4 [11]

$$n_{\text{Si}_3\text{N}_4}^2 = 1 + \frac{3.0249\lambda^2}{\lambda^2 - 135.3406^2} + \frac{40314\lambda^2}{\lambda^2 - 1239842^2} \qquad (3.8)$$

14

It is plotted in Figure 8.6 , along with the material dispersion parameter D_M. This equation is valid over the wavelength range 310–5504 nm.

On the other hand, the numerical simulation is adopted to evaluate the dispersion parameter, then according to the second-order dispersion chain rule in Equation 3.6,

3.3 DISPERSION ENGINEERING USING SLOT STRUCTURE

Using the commercial Comsol Multiphysics package for FEM simulations, we implemented a 2D simulation which takes into account the cylindrical symmetry of the system in the third dimension. Material dispersion is taken into account via an iterative approach which takes the values of the refractive index from measured values for our SiN films. The values for dispersion parameters are obtained from fitting appropriate polynomials to the absolute frequencies of the modes around our pump wavelength of 192.2 THz. The relative magnitude of the values for the free spectral range in the simulation is used to identify the mode

3.4 EFFECTS OF MODE CROSSING

Chapter 4

Device fabrication of silicon nitride ring cavities

4.1 FABRICATION PROCESS USING SUBTRACTIVE METHOD

4.1.1 Material properties

4.1.2 Patterning and etching

4.1.3 Optical I/O and packaging

4.2 FABLESS SAMPLES VIA FOUNDRIES

Chapter 5

Dispersion evaluation from transmission spectroscopy

5.1 Methods

5.2 Setups

5.3 Result of SiNx (cf. Hydex) device dispersion

Chapter 6

Broadband Photon pair generation

6.1 Joint spectrum intensity

6.2 Coincidence counts vs. pump

6.3 Coincidence counts vs. pump

Chapter 7

Towards intermodal and intramodal photon pair

7.1 SPONTANEOUS FOUR WAVE MIXING

7.2 STIMULATED FOUR WAVE MIXING

Chapter 8

Summary

Acknowledgements

Nam dui ligula, fringilla a, euismod sodales, sollicitudin vel, wisi. Morbi auctor lorem non justo. Nam lacus libero, pretium at, lobortis vitae, ultricies et, tellus. Donec aliquet, tortor sed accumsan bibendum, erat ligula aliquet magna, vitae ornare odio metus a mi. Morbi ac orci et nisl hendrerit mollis. Suspendisse ut massa. Cras nec ante. Pellentesque a nulla. Cum sociis natoque penatibus et magnis dis parturient montes, nascetur ridiculus mus. Aliquam tincidunt urna. Nulla ullamcorper vestibulum turpis. Pellentesque cursus luctus mauris.

Nulla malesuada porttitor diam. Donec felis erat, congue non, volutpat at, tincidunt tristique, libero. Vivamus viverra fermentum felis. Donec nonummy pellentesque ante. Phasellus adipiscing semper elit. Proin fermentum massa ac quam. Sed diam turpis, molestie vitae, placerat a, molestie nec, leo. Maecenas lacinia. Nam ipsum ligula, eleifend at, accumsan nec, suscipit a, ipsum. Morbi blandit ligula feugiat magna. Nunc eleifend consequat lorem. Sed lacinia nulla vitae enim. Pellentesque tincidunt purus vel magna. Integer non enim. Praesent euismod nunc eu purus. Donec bibendum quam in tellus. Nullam cursus pulvinar lectus. Donec et mi. Nam vulputate metus eu enim. Vestibulum pellentesque felis eu massa.

Quisque ullamcorper placerat ipsum. Cras nibh. Morbi vel justo vitae lacus tincidunt ultrices. Lorem ipsum dolor sit amet, consectetuer adipiscing elit. In hac habitasse platea dictumst. Integer tempus convallis augue. Etiam facilisis. Nunc elementum fermentum wisi. Aenean placerat. Ut imperdiet, enim sed gravida sollicitudin, felis odio placerat quam, ac pulvinar elit purus eget enim. Nunc vitae tortor. Proin tempus nibh sit amet nisl. Vivamus quis tortor vitae risus porta vehicula.

References

1. Wengerowsky, S., Joshi, S. K., Steinlechner, F., Hübel, H. & Ursin, R. An entanglement-based wavelength-multiplexed quantum communication network. *Nature* **564,** 225–228 (2018).

2. Tchebotareva, A. *et al.* Entanglement between a Diamond Spin Qubit and a Photonic Time-Bin Qubit at Telecom Wavelength. *Phys. Rev. Lett.* **123,** 063601 (2019).

3. Okano, M. *et al.* 0.54 um Resolution Two-Photon Interference With Dispersion Cancellation for Quantum Optical Coherence Tomography. *Sci. Rep.* **5,** 1–8 (2015).

4. Lu, X., Jiang, W. C., Zhang, J. & Lin, Q. Biphoton Statistics of Quantum Light Generated on a Silicon Chip. *ACS Photonics* **3,** 1626–1636 (2016).

5. Bogaerts, W. *et al.* Silicon microring resonators. *Laser Photonics Rev.* **6,** 47–73 (2012).

6. Ono, Y. *A study of photon-pair generation using silicon nitride ring resonators* Master Thesis (Kyoto University, 2017).

7. Pfeiffer, M. H., Liu, J., Geiselmann, M. & Kippenberg, T. J. Coupling Ideality of Integrated Planar High- Q Microresonators. *Phys. Rev. Appl.* **7,** 1–8 (2017).

8. Leuthold, J., Koos, C. & Freude, W. Nonlinear silicon photonics. *Nat. Photonics* **4,** 535–544 (2010).

9. Agrawal, G. in *Nonlinear Fiber Optics (Fifth Edition)* (ed Agrawal, G.) Fifth Edition, 397–456 (Academic Press, Boston, 2013).

10. Brasch, V. *et al.* Photonic chip-based optical frequency comb using soliton Cherenkov radiation. *Science (80-.).* **351,** 357–360 (2016).

11. Luke, K., Okawachi, Y., Lamont, M. R. E., Gaeta, A. L. & Lipson, M. Broadband mid-infrared frequency comb generation in a Si_3N_4 microresonator. *Opt. Lett.* **40,** 4823 (2015).
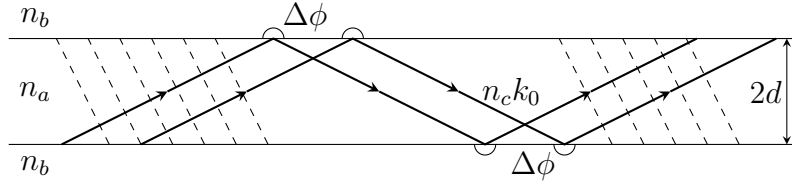
List of Figures

Figure 8.1: **Planar waveguide**. The upper and bottom layer are cladding and the middle is core layer. $\Delta\phi$ represents the Goos-Hänchen shift at the boundary.
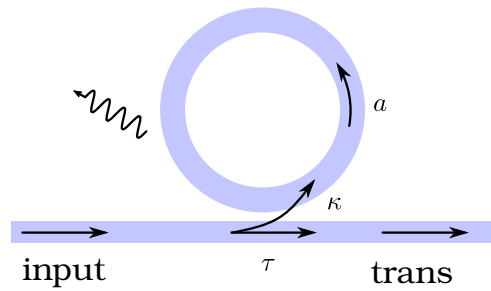

Figure 8.2: **An all-pass type ring resonator**. The transmitted spectrum is filtered periodically by the ring waveguide, in the case satisfying resonance condition.
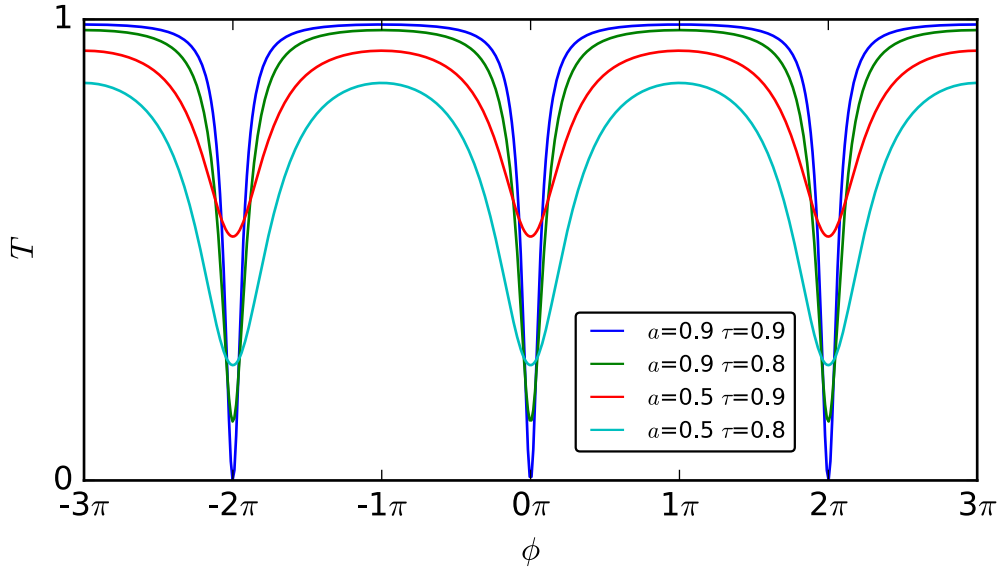
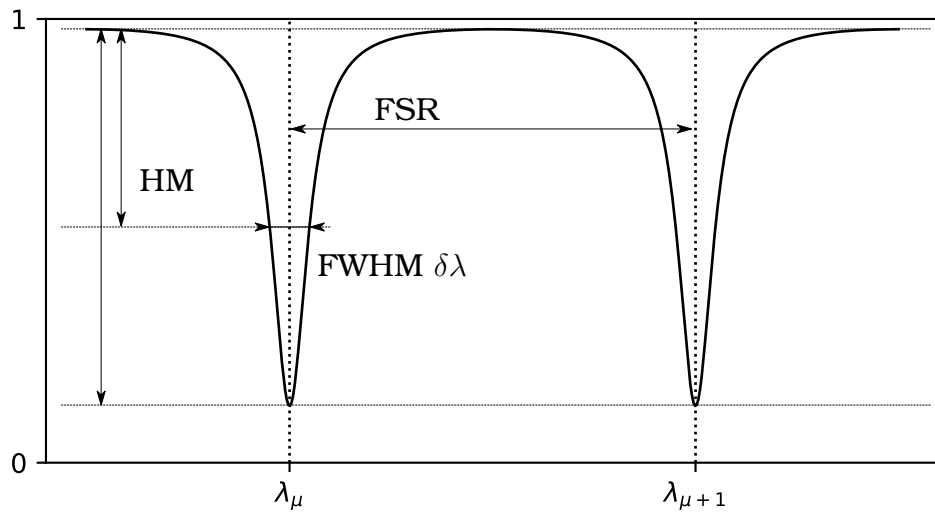Figure 8.3: **The transmission spectrum of a ring resonator**.

Figure 8.4: **Illustration of wavelength transmission spectrum of ring resonators**. FSR, free spectral range, the distance between neighbouring resonant wavelength. FWHM, full width at half maximum.
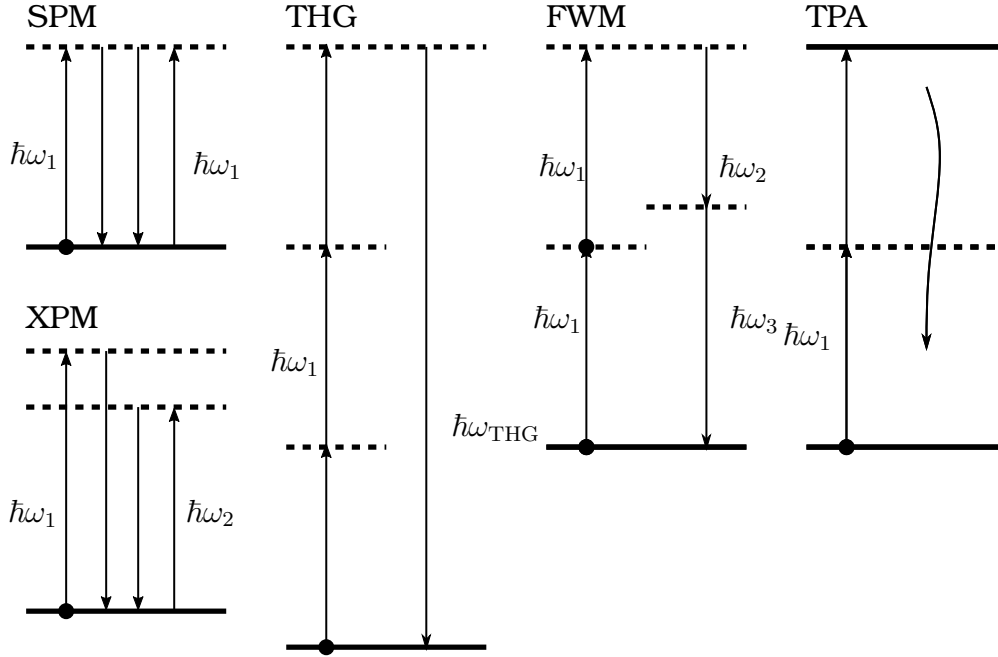
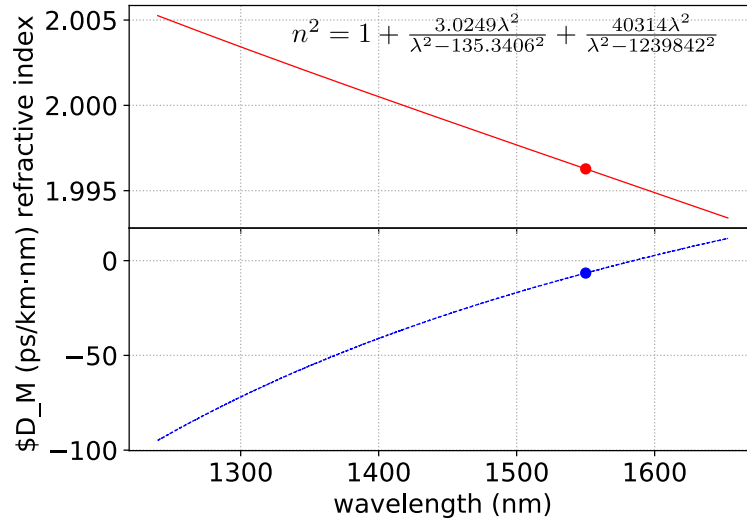Figure 8.5: **Illustration of possible energy diagram in typical third-order nonlinear processes**.

$$n^2 = 1 + \frac{3.0249\lambda^2}{\lambda^2 - 135.3406^2} + \frac{40314\lambda^2}{\lambda^2 - 1239842^2}$$

Figure 8.6: **Refractive index and dispersion parameter measured in reference**. λ=1550 nm, n=1.9963 and D_M = -6.57 ps/km·nm .

Appendix A

Dispersion simulation

Appendix B

Layout design